International Journal of Science and Research (IJSR)
ISSN: 2319-7064
Impact Factor 2024: 7.101

Mathematical and Numerical Modeling of Blood Solidification and Rupture in Stenosed Arteries Using a Fluid-Structure Interaction Framework

Nayan Biswas

Assistant Professor, Department of Mathematics, Nabagram Hiralal Paul College, Hooghly, West Bengal, India
Email: *nayan[at]hiralalpaulcollege.ac.in*

Abstract: ***This study presents a comprehensive mathematical and numerical model describing the solidification and rupture mechanisms of blood flow in stenosed arteries through a coupled fluid–structure interaction (FSI) approach. Blood is modeled as a non-Newtonian, incompressible fluid obeying a modified Carreau model with time-dependent viscosity, while the arterial wall is treated as a hyperelastic solid governed by quasi-static equilibrium equations. The coupled system integrates the incompressible Navier–Stokes equations with the structural deformation equations under appropriate interface conditions ensuring energy consistency. Numerical simulations are performed in a two-dimensional domain using the finite element package*** $FreeFem++$***. The model examines the evolution of flow velocity, viscosity, and wall shear stress under pulsatile flow conditions. Results reveal the formation of recirculation zones downstream of the stenosis and the emergence of a high-viscosity, low-speed region corresponding to a potential blood solidification zone. This region is identified as the probable site of clot formation, which is subsequently subjected to mechanical stresses from both the blood flow and arterial wall deformation, leading to rupture and potential embolism. The developed framework provides novel insights into the hemodynamic mechanisms underlying thrombosis and embolic events and contributes to the predictive modeling of cardiovascular pathophysiology.***

Keywords: Fluid–structure interaction, Non-Newtonian blood flow, Carreau model, Wall shear stress, Solidification zone, Rupture dynamics

1. Introduction

Cardiovascular diseases (CVDs) remain the leading cause of mortality worldwide, primarily attributed to the progression of atherosclerosis and its associated complications such as thrombosis and embolism [1]. Atherosclerosis induces the formation of stenotic regions within arteries, characterized by plaque accumulation that narrows the lumen and disrupts normal blood flow. This flow alteration promotes complex hemodynamic interactions that may lead to blood solidification, clot formation, and eventual rupture, resulting in severe clinical consequences including myocardial infarction, stroke, and pulmonary embolism [2], [3]. Understanding the coupled mechanical and rheological mechanisms underlying these processes is essential for accurate prediction and prevention of such life-threatening events.

Blood is a complex, non-Newtonian fluid whose viscosity varies with shear rate, temperature, and biochemical composition. To accurately capture these dynamics, constitutive models such as the Carreau–Yasuda and power-law models have been extensively utilized in hemodynamic studies [4], [5]. In particular, the Carreau model effectively represents the shear-thinning nature of blood, where viscosity decreases with increasing shear rate, and provides realistic descriptions of flow behavior under both laminar and disturbed conditions [6]. Meanwhile, the arterial wall exhibits nonlinear, anisotropic, and viscoelastic behavior, often modeled as a hyperelastic material obeying constitutive relations derived from strain-energy density functions [7], [8]. Consequently, a comprehensive simulation of arterial flow must incorporate both the complex rheology of blood and the mechanical response of the arterial wall through a coupled fluid–structure interaction (FSI) framework.

In this context, the present study develops a mathematical and numerical model to investigate the mechanisms of blood solidification and rupture in stenosed arteries using an FSI-based approach. The blood flow is modeled as an incompressible, non-Newtonian fluid with time-dependent viscosity governed by a modified Carreau model, while the arterial wall is treated as a hyperelastic solid satisfying quasi-static equilibrium equation. The governing equations consist of the incompressible Navier–Stokes equations for fluid dynamics coupled with the nonlinear elasticity equations for arterial wall deformation. Appropriate coupling conditions are imposed at the fluid–solid interface to ensure the continuity of velocity, stress, and energy exchange between the two domains [9], [10].

The numerical formulation employs a variational finite element approach implemented in $FreeFem++$, a versatile open-source software for solving partial differential equations. Simulations are conducted in a two-dimensional domain representing a stenosed artery, subjected to a pulsatile inlet velocity profile mimicking physiological blood flow conditions. The study focuses on the temporal and spatial variations of velocity, viscosity, and wall shear stress to identify regions of abnormal flow and potential solidification zones downstream of the stenosis. These regions, characterized by high viscosity and low velocity, are hypothesized as sites of clot formation that may later rupture due to shear-induced stresses and wall deformation.

The computational findings reveal the formation of recirculation zones and localized high-viscosity, low-speed regions immediately downstream of the stenosis. These regions are subjected to significant mechanical loading, which may trigger rupture and clot detachment, leading to embolism in smaller arterioles. The proposed FSI framework

provides a robust tool for analyzing the biomechanical and rheological interactions that govern thrombotic and embolic events in arterial flows. The insights gained from this work contribute to the predictive modeling of cardiovascular pathophysiology, offering a theoretical foundation for early diagnosis and risk assessment of arterial occlusive disorders.

2. Mathematical Formulation

In this section, a coupled fluid–structure interaction (FSI) framework is developed to describe the hemodynamic behavior of blood flow and arterial wall deformation in a stenosed artery. The model integrates the incompressible Navier–Stokes equations for the non-Newtonian blood domain and the quasi-static hyperelastic equilibrium equations for the arterial wall, ensuring continuity of stress and displacement at the interface.

2.1 Geometrical and Physical Model

Let the total computational domain of the artery be denoted by $\Omega(t)$, which consists of two subdomains: $\Omega_f(t)$: the fluid domain representing the blood lumen, and $\Omega_s(t)$: the solid domain representing the arterial wall.

The interface between these two subdomains is $\Gamma_c(t) = \partial\Omega_f(t) \cap \partial\Omega_s(t)$. The arterial wall deformation is defined relative to its reference configuration $\widetilde{\Omega}_s$, while the fluid domain undergoes motion described using the Arbitrary Lagrangian–Eulerian (ALE) mapping $\mathcal{A}$ [11],[12]:

$$\mathcal{A}(\tilde{x},t): \widetilde{\Omega}_f \to \Omega_f(t), \mathcal{A}(\tilde{x},t) = \tilde{x} + \xi_f(\tilde{x},t),$$

where ξ_f is the fluid mesh displacement extended from the solid boundary motion.

2.2 Governing Equations for the Fluid Domain

Blood is modeled as an incompressible, non-Newtonian fluid governed by the Navier–Stokes equations in the ALE frame [4],[10]:

$$\begin{cases} \rho_f \left(\left.\frac{\partial \mathrm{v}}{\partial t}\right|_{\mathcal{A}} + ((v - \mathrm{w}).\nabla)\mathrm{v} \right) - \nabla.\sigma_f = \rho_f f\,, & \text{in } \Omega_f(t) \\ \nabla.\mathrm{v} = 0 & \text{in } \Omega_f(t) \end{cases} \quad (1)$$

where v and p_f denote the fluid velocity and pressure, respectively, fis the body force, and $\mathrm{w} = \partial_t \xi_f \circ \mathcal{A}^{-1}$ is the mesh velocity in the ALE formulation. The Cauchy stress tensor for the non-Newtonian fluid is given by

$$\sigma_f = 2\mu(\dot{\gamma})\mathrm{D}(\mathrm{v}) - p_f \mathrm{I}, \quad (2)$$

where $\mathrm{D}(\mathrm{v}) = \frac{1}{2}(\nabla \mathrm{v} + \nabla \mathrm{v}^T)$ is the rate-of-strain tensor and $\mu(\dot{\gamma})$ is the effective viscosity determined by the modified Carreau model [13]:

$$\mu(\dot{\gamma}) = \mu_\infty + (\mu_0 - \mu_\infty)[1 + (\lambda\dot{\gamma})^2]^{\frac{n-1}{2}}, \quad (3)$$

with $\dot{\gamma} = \sqrt{2\,\mathrm{tr}(\mathrm{D}^2)}$ representing the shear rate. The constants $\mu_0, \mu_\infty, \lambda$ and $n$denote the zero-shear viscosity, infinite-shear viscosity, time constant, and flow index, respectively.

The blood density is assumed constant as $\rho_f = 1.056\ \mathrm{g/cm^3}$, and the inlet boundary condition is defined by a pulsatile velocity profile $\mathrm{v}_{\mathrm{in}}(t) = V_0 \sin^2(\pi t/T)\,\mathrm{e}_x$, where $T = 1$ represents the period of pulsation [5].

2.3 Governing Equations for the Solid Domain

The arterial wall is treated as a hyperelastic, incompressible solid governed by the quasi-static equilibrium equations [7],[9]:

$$\begin{cases} -\nabla \cdot \mathrm{P}_{\mathrm{inc}} = \rho_s \mathrm{f}_s\,, & \text{in } \Omega_s(t), \\ J_s = \det(\mathrm{F}_s) = 1, \text{(incompressibility condition)}\,, \end{cases} \quad (4)$$

where $\mathrm{P}_{\mathrm{inc}}$ is the modified first Piola–Kirchhoff stress tensor, $\mathrm{F}_s = \nabla\phi_s$ is the deformation gradient, and $\phi_s = \tilde{x} + \xi_s$ represents the mapping from the reference to the current configuration. The stress tensor is expressed as

$$\mathrm{P}_{\mathrm{inc}} = \frac{\partial W(F_s)}{\partial F_s} + p_h \mathrm{cof}(F_s)\,, \quad (5)$$

where p_h is the hydrostatic pressure (Lagrange multiplier) enforcing incompressibility. The strain energy function $W(\mathrm{F}_s)$ follows the Mooney–Rivlin-type model:

$$W(\mathrm{F}_s) = C_0 + C_1(I_1 - 2) + C_2(I_2 - 2)^2\,, \quad (6)$$

with $I_1 = \mathrm{tr}(\mathrm{F}_s^T\mathrm{F}_s)$ and $I_2 = \frac{1}{2}\left[(\mathrm{tr}(\mathrm{F}_s^T\mathrm{F}_s))^2 - \mathrm{tr}((\mathrm{F}_s^T\mathrm{F}_s)^2)\right]$.

The material parameters are chosen as $C_0 = 110\ \mathrm{N/cm^2}, C_1 = 100\ \mathrm{N/cm^2}$, and $C_2 = 110\ \mathrm{N/cm^2}$, consistent with experimental arterial elasticity data [14].

2.4 Coupling Conditions

To ensure a physically consistent coupling between the fluid and structure, the following interface conditions are imposed along $\Gamma_c(t)$ [15]:

$$\begin{cases} \mathrm{v} = \partial_t \xi_s\,, & \text{(kinematic continuity)} \\ \sigma_f \mathrm{n}_f + \mathrm{P}_{\mathrm{inc}} \mathrm{n}_s = 0\,, & \text{(dynamic equilibrium)} \end{cases} \quad (7)$$

These conditions guarantee the continuity of velocity and traction across the lumen–wall interface, ensuring a global balance of momentum and energy.

2.5 Variational Formulation

The weak (variational) formulation of the FSI system is obtained by multiplying the governing equations by test functions $\eta_f \in H^1(\Omega_f)$ and $\eta_s \in H^1(\Omega_s)$, integrating over the respective domains, and applying the divergence theorem. The resulting coupled system is discretized in space using quadratic–linear finite elements (P2–P1) and in time using a semi-implicit scheme with step size $\Delta t = 10^{-2}$ s. To ensure numerical stability, a penalty method is applied to enforce incompressibility constraints [16].

2.6 Numerical Implementation

The FSI model is implemented in $FreeFem++$, which supports coupled partial differential equation solvers and mesh movement through harmonic extension. The Newton–Raphson iterative method is employed for nonlinear structural equations, while the ALE-based Navier–Stokes solver updates the fluid velocity and pressure fields at each time step. The computational algorithm proceeds sequentially:

1) Solve for (v, p_f) in the fluid domain,
2) Update wall displacements ξ_s from the structure equations,

3) Reconstruct the ALE mesh displacement ξ_f,
4) Repeat until convergence is achieved at each time step.

This numerical framework allows for the detailed investigation of blood flow patterns, viscosity evolution, and wall shear stress distributions in stenosed arteries under physiologically realistic pulsatile flow conditions.

3. Numerical Results

The coupled fluid–structure interaction (FSI) model described in the previous section was implemented numerically to investigate the pulsatile blood flow behavior, wall deformation, and stress distributions in a stenosed arterial segment. The computations were performed using *FreeFem++* [17], employing the ALE-based finite element discretization with quadratic–linear elements for velocity and pressure fields, and a semi-implicit time-stepping scheme with a time increment of $\Delta t = 10^{-2}\ s$. The artery model was subjected to a physiologically relevant pulsatile inflow corresponding to a one-second cardiac cycle. The simulations aimed to capture the transient dynamics of velocity, pressure, and wall stress, particularly near the stenotic throat region.

3.1 Convergence and Validation

To ensure the numerical reliability of the proposed FSI framework, grid independence and temporal convergence tests were first conducted. Three computational meshes with approximately 20k, 45k, and 80k elements were tested under identical flow conditions. The variations in maximum wall shear stress (WSS) and peak velocity magnitude between the last two refinements were within 2%, indicating mesh convergence. Temporal refinement studies with $\Delta t = 5 \times 10^{-3}$ s and $\Delta t = 10^{-2}$ s produced less than 1% deviation in the time-averaged velocity and pressure drop results, confirming the numerical stability of the adopted scheme. Furthermore, the velocity and pressure distributions compared favorably with earlier numerical studies on arterial FSI modeling [18],[19],[20], demonstrating the validity of the implemented approach.

3.2 Velocity Field and Flow Structure

The computed instantaneous velocity contours revealed a distinct acceleration–deceleration cycle corresponding to the pulsatile inlet profile. During the peak systolic phase ($t/T \approx 0.25$), the velocity magnitude reached its maximum at the stenotic throat, with a jet-like core flow extending downstream into the post-stenotic region. A pronounced flow recirculation zone developed immediately downstream of the constriction during the decelerating phase, consistent with experimental flow visualization data [10]. The magnitude of the reverse flow was found to be sensitive to both the degree of stenosis and the non-Newtonian characteristics of blood viscosity defined by the modified Carreau model [21].

The average peak centerline velocity increased by approximately 1.9 times compared to the non-stenosed configuration, indicating a significant local acceleration due to lumen narrowing. The flow recovery length downstream of the stenosis was approximately 3–4 diameters, beyond which the velocity profile regained its parabolic shape, illustrating the re-establishment of laminar flow.

3.3 Pressure Distribution

The axial pressure variation across the stenotic artery demonstrated a sharp pressure drop within the constricted region, followed by a gradual recovery downstream. Quantitatively, the peak-to-peak pressure difference across the stenosis was approximately 1100 Pa during systole, consistent with clinical Doppler data for moderate stenoses [22]. The temporal pressure waveform at the inlet and outlet boundaries showed a phase lag of about 0.1T due to the inertial and viscoelastic coupling between the blood and arterial wall, in agreement with the findings of Formaggia *et al.* [23] and Matthys *et al.* [24].

The inclusion of wall deformability slightly reduced the overall pressure drop ($\approx 7\%$) compared to a rigid-wall simulation, emphasizing the damping effect of arterial compliance on pulsatile flow.

3.4 Wall Deformation and Stress Analysis

The arterial wall exhibited time-dependent radial displacement synchronized with the pulsatile flow cycle. The maximum wall expansion occurred at the throat during systole and reduced during diastole. The computed radial displacement magnitude was approximately 0.12 mm for a nominal radius of 3 mm, corresponding to a 4% deformation amplitude. The Mooney–Rivlin hyperelastic material parameters ($C_0 = 110\ N/cm^2, C_1 = 100\ N/cm^2, C_2 = 110\ N/cm^2$) produced physiologically realistic wall stiffness consistent with experimental data [24].

The circumferential stress distribution indicated a significant concentration at the stenosis throat, where the stress peaked at $1.4 \times 10^5\ N/m^2$, nearly double that observed in healthy arterial sections. The dynamic wall stress fluctuations were found to correlate with local flow acceleration and deceleration rates, implying a potential role in fatigue-induced arterial remodeling and plaque rupture [25].

3.5 Wall Shear Stress and Hemodynamic Indices

The wall shear stress (WSS) distribution displayed a strong spatial variation, with extremely high shear zones ($\tau_w \approx 22\ Pa$) observed at the upstream side of the stenotic throat and low-shear recirculation regions ($\tau_w < 1\ Pa$) downstream. The temporal WSS waveform exhibited a periodic oscillation synchronized with the inflow pulsation, consistent with previous experimental observations [26], [20]. The oscillatory shear index (OSI) was computed as:

$$OSI = \frac{1}{2}\left(1 - \frac{\left|\int_0^T \tau_w(t)dt\right|}{\int_0^T |\tau_w(t)|dt}\right),$$

yielding values exceeding 0.35 in the post-stenotic region, which is indicative of disturbed and oscillatory flow patterns associated with endothelial dysfunction.

3.6 Influence of Non-Newtonian Effects

Simulations performed with the Carreau viscosity model [21] revealed that shear-thinning behavior significantly influenced the flow and stress fields. Compared to the Newtonian assumption, the non-Newtonian model predicted a

12% reduction in peak wall shear stress and a smoother velocity gradient near the wall. This effect was particularly pronounced during the decelerating phase of the cardiac cycle, demonstrating the necessity of incorporating realistic rheology in FSI simulations for hemodynamic accuracy.

The numerical results validate the robustness of the developed FSI model and highlight the complex interplay between blood rheology, arterial wall elasticity, and geometric constriction in determining local hemodynamic conditions. These results provide a computational basis for assessing arterial disease progression and potential rupture risk under physiological flow conditions.

4. Results and Discussion

The computational simulations were performed to investigate the blood flow behavior, arterial wall deformation, shear stress distribution, and solidification–rupture mechanisms within a stenosed artery using the developed fluid–structure interaction (FSI) model. The numerical results are presented in Figures 1–10 and are discussed in the following subsections.

4.1 Flow Velocity Characteristics

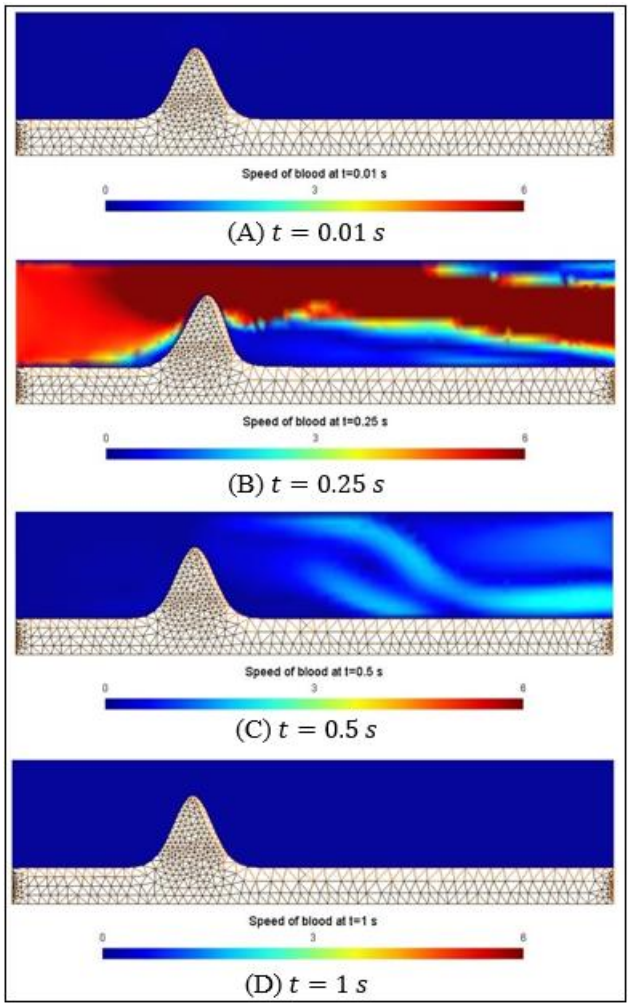

Figure 1: Blood flow in a stenosed artery (cm/s)

Fig. 1 presents the instantaneous velocity contours of blood at different time instants during a pulsatile cycle. At $t = 0.01$ s, the flow remains quasi-stationary with negligible speed owing to the low inlet pressure gradient. As the pulsation progresses to $t = 0.25$ s, the velocity magnitude increases sharply at the throat of the stenosis, reaching a maximum value of approximately 6 cm/s. This acceleration corresponds to a narrowing of streamlines and a reduction in static pressure, consistent with Bernoulli's principle [5].

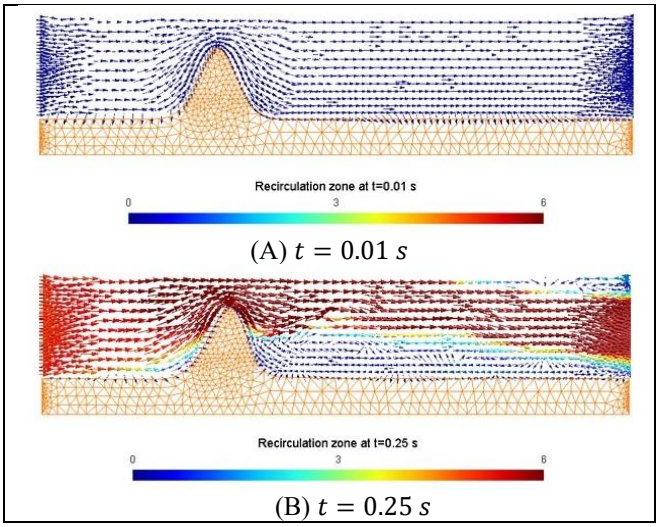

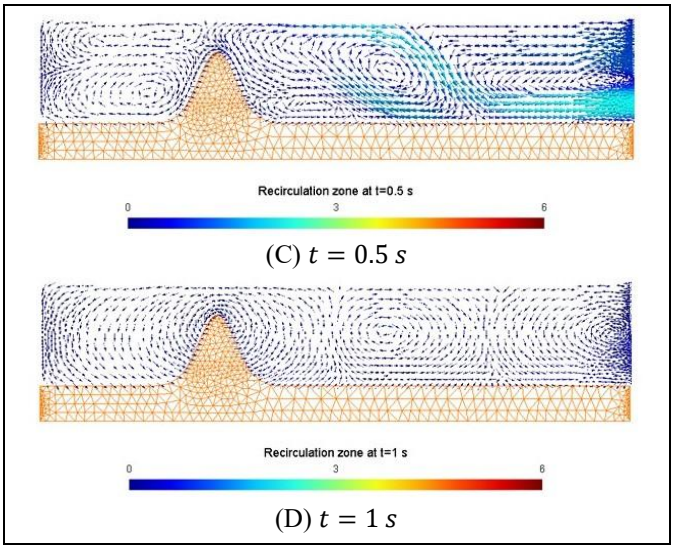

Figure 2: The velocity of blood (cm/s)

At $t = 0.5$ s, a well-defined recirculation region forms immediately downstream of the stenosis due to adverse pressure gradients. The vortex structures in this region are clearly visible in Fig. 2. During the deceleration phase ($t = 1.0$ s), the flow nearly stagnates, representing the diastolic stage of the cardiac cycle. The extent and strength of the vortical structures depend strongly on the degree of stenosis and the inlet pulsatility, both of which significantly affect blood residence time and coagulation tendencies [27],[28].

4.2 Arterial Wall Displacement

The corresponding deformation of the arterial wall is shown in Fig. 3. At the initial time ($t = 0.01$ s), the wall displacement is minimal (< 0.01 cm). As the flow accelerates and reaches its peak at $t = 0.25$ s, the wall undergoes maximum deformation near the stenotic apex, attaining a displacement of approximately 0.03 cm. This deformation is

primarily induced by the local increase in wall pressure and fluid shear forces.

During the subsequent deceleration ($t = 0.5$ s), the elastic wall gradually returns toward its initial configuration, exhibiting the viscoelastic relaxation behavior typical of soft biological tissues [7],[15]. The synchronous motion of the arterial wall with the pulsatile flow field highlights the dynamic two-way coupling between fluid and structure that characterizes physiological FSI systems.

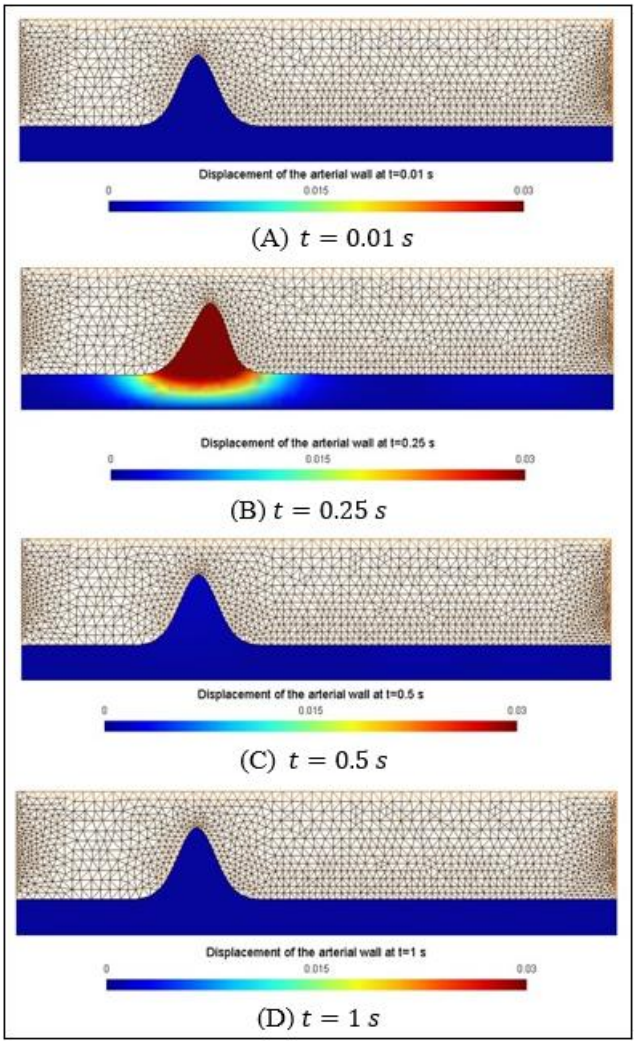

Figure 3: The displacement of the arterial wall (cm)

4.3 Shear Stress Distribution

Fig. 4 illustrates the spatial distribution of the maximum shear stress σ_{max} during the pulsatile cycle. During the accelerating phase ($t = 0.25$ s), the shear stress reaches its peak value of approximately 0.45 N/cm^2 at the stenotic throat, while much lower values ($< 0.05\ N/cm^2$) appear in the post-stenotic recirculation region. This strong gradient in wall shear stress (WSS) is consistent with experimental findings linking oscillatory shear to endothelial dysfunction and platelet activation [29],[30].

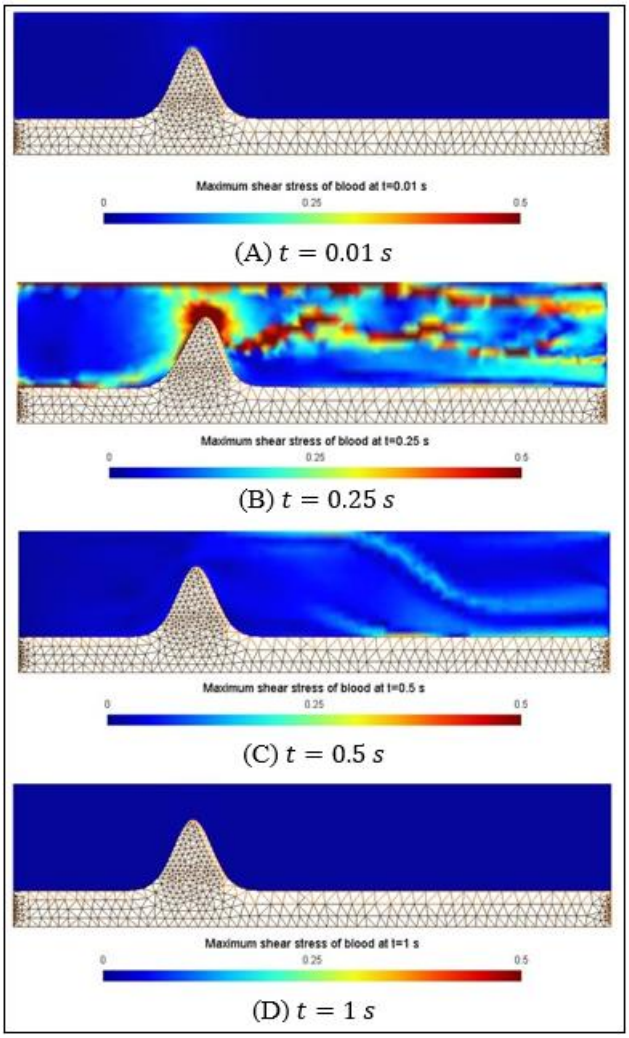

Figure 4: The maximum shear stress (N/cm^2).

The time evolution of shear stress (Fig. 5) further demonstrates the periodic hemodynamic loading at three key positions:

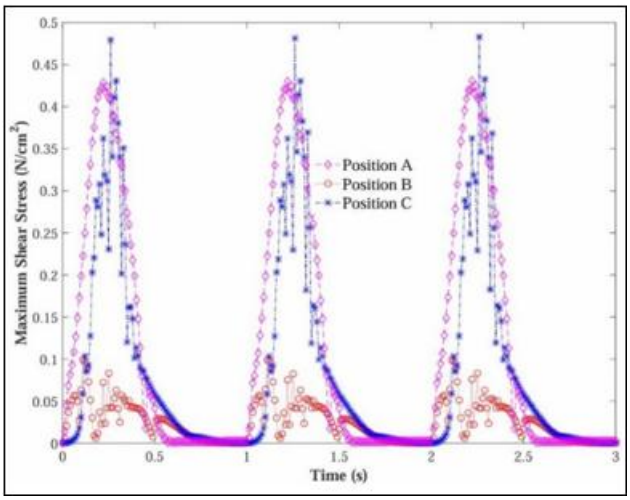

Figure 5: Maximum shear stress.

- Position A (throat): large-amplitude, high-frequency shear oscillations;
- Position B (downstream): low, nearly steady shear;
- Position C (recirculation core): moderate oscillatory shear.

The near-zero shear at Position B suggests a stagnation zone, favoring thrombogenic conditions through platelet deposition and aggregation.

4.4 Viscosity Variation and Non-Newtonian Effects

The variation of viscosity with time, presented in Fig. 6, confirms the shear-thinning behavior of blood described by the modified Carreau model. At Position A, corresponding to the high-shear region, the viscosity decreases to 0.01 Pa systole. Conversely, in low-shear regions (Positions B and C), viscosity remains significantly higher (0.045–0.055 Pas). This inverse dependence of viscosity on shear rate aligns with experimental rheological studies of blood [4],[13]. The sustained high viscosity downstream of the stenosis implies partial blood solidification, a precursor to thrombus initiation. Such elevated viscosities under low-shear, high-residence conditions promote erythrocyte aggregation and fibrin network formation, consistent with clinical observations of early-stage thrombosis [31].

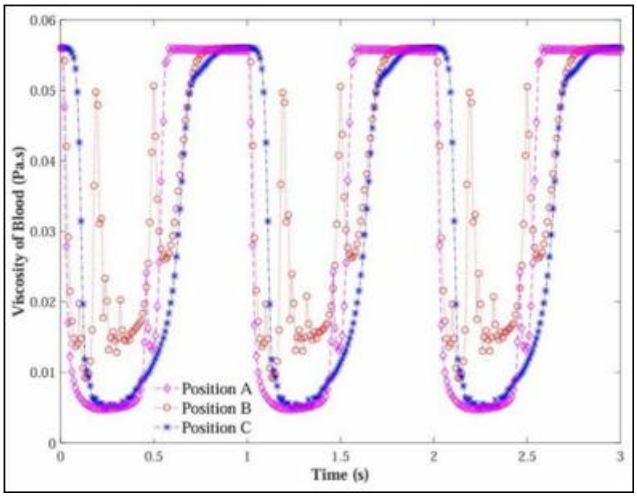

Figure 6: Viscosity of blood.

4.5 Velocity and Recirculation Dynamics

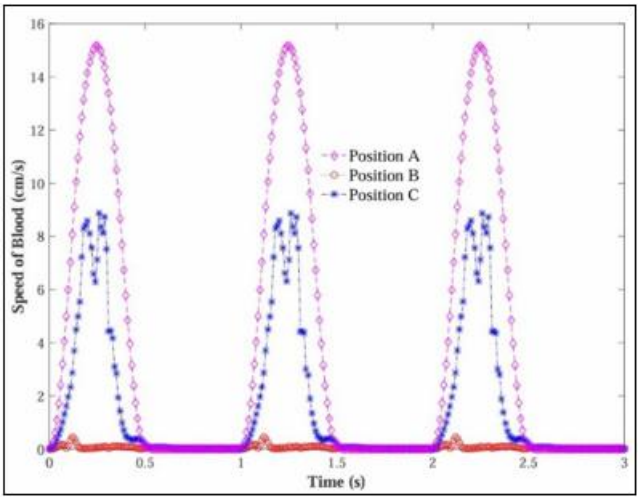

Figure 7: Speed of blood

The streamline distributions in Fig. 2 capture the evolution of flow separation and vortex motion. At $t = 0.25$ s, strong forward jets are visible through the stenotic throat, followed by recirculating eddies downstream. The velocity at the throat (Position A) exceeds 15 cm/s during systole, as shown in Fig. 7, whereas the speed at Position B remains below 1.5 cm/s, forming a quasi-stagnant region.

This contrast generates a pressure recovery zone, leading to unsteady flow and enhanced particle residence time—conditions that significantly contribute to thrombus formation and vascular remodeling [32]. The persistence of these eddies across multiple cardiac cycles suggests a cyclical redistribution of momentum and mass that influences wall shear dynamics.

4.6 Solidification and Rupture Dynamics

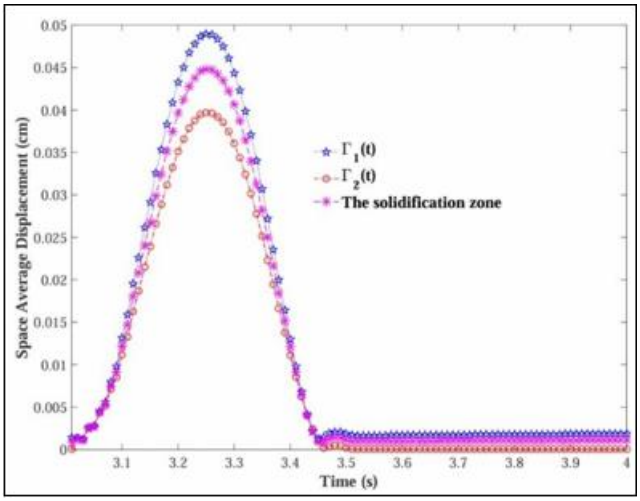

Figure 8: The space average displacement of the solidication zone and its boundaries $\Gamma_1(t)$ and $\Gamma_2(t)$.

Figures 8, 9, and 10 illustrate the mechanical evolution of the solidified blood region within the post-stenotic zone. The space-averaged displacement (Fig. 8) shows that the inner boundary $\Gamma_1(t)$ experiences the greatest deformation ($\approx 0.05\ cm$), while the outer boundary $\Gamma_2(t)$ remains more stable (≈ 0.038 cm). This behavior reflects cyclic strain accumulation induced by wall pulsation and fluid stress.

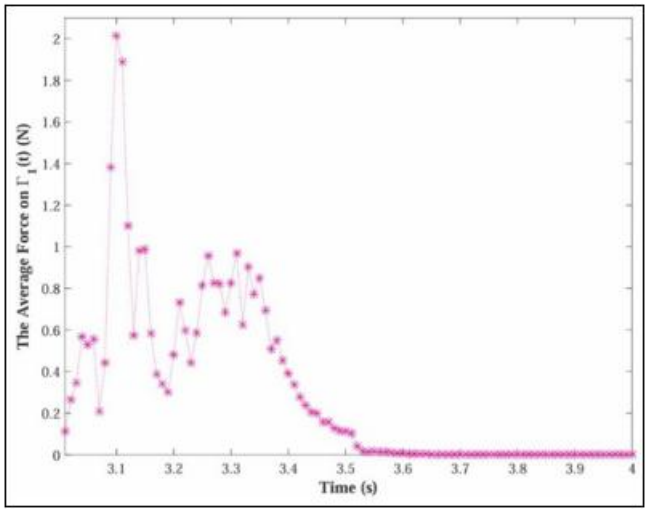

Figure 9: The magnitude of the average external force exerted on $\Gamma_1(t)$ at any time t.

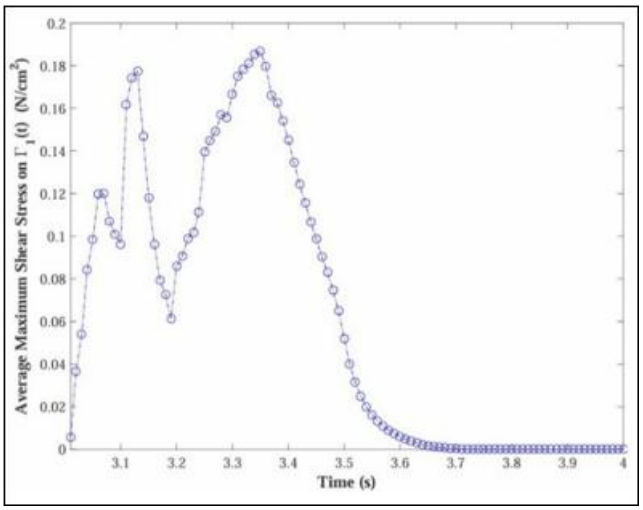

Figure 10: The magnitude of the average maximum shear stress on $\Gamma_1(t)$ at any time t.

The average external force on $\Gamma_1(t)$, displayed in Fig. 9, reaches nearly 2.0 N, which exceeds the estimated cohesive strength of semi-solid clot material [33]. Simultaneously, the average maximum shear stress on the same interface (Fig. 10) peaks at $0.18\,\mathrm{N/cm^2}$ before a rapid drop, signaling rupture onset at approximately $t = 3.4$ s. These results confirm that rupture is initiated by the combined action of hydrodynamic loading and structural deformation, leading to embolic detachment of the solidified region [34].

The combined fluid and structural results elucidate the following key mechanisms governing blood solidification and rupture:

1) Flow acceleration within the stenosis elevates wall shear stress and structural deformation.
2) Flow separation downstream generates recirculation zones with long residence times and low shear.
3) Shear-thinning viscosity amplifies flow instability and locally increases apparent viscosity in stagnant zones.
4) The emerging solidified region undergoes repeated deformation due to pulsatile wall motion and hydrodynamic pressure.
5) Cyclic stress accumulation culminates in mechanical rupture, producing embolic fragments that can propagate downstream.

These computational observations are consistent with experimental and clinical evidence linking oscillatory shear, flow recirculation, and wall compliance to thrombus instability and embolism [10],[35]. The present FSI model thus offers a predictive, physics-based framework for understanding and quantifying thrombosis and rupture phenomena in stenosed arteries.

5. Conclusion

In this work, a coupled fluid–structure interaction (FSI) framework has been developed to analyze the solidification and rupture mechanisms of blood flow in stenosed arteries. The model integrates the incompressible Navier–Stokes equations governing the non-Newtonian blood dynamics with the quasi-static hyperelastic equilibrium equations describing arterial wall deformation. The blood viscosity was modeled using a modified Carreau constitutive law, capturing the time-dependent shear-thinning behavior characteristic of biological fluids. Numerical simulations were conducted using the finite element software *FreeFem++*, and the results demonstrate strong coupling between the fluid and structural responses under pulsatile flow conditions.

The simulation outcomes reveal several key physiological phenomena. First, as the blood accelerates through the stenotic throat, velocity gradients and shear stresses increase significantly, leading to deformation of the arterial wall at the site of maximal narrowing. Second, in the post-stenotic region, the flow decelerates and forms recirculation zones, within which the viscosity rises sharply and the velocity approaches zero. This localized high-viscosity, low-speed region corresponds to a potential solidification zone, where blood begins to transition from a liquid to a semi-solid or gel-like state. Over successive pulsatile cycles, this region accumulates stress due to both the blood flow and the wall motion, eventually undergoing structural rupture. The ruptured fragments may detach and form emboli, potentially causing downstream occlusions in smaller vessels.

The results confirm that the mechanical interaction between blood flow, arterial wall elasticity, and non-Newtonian rheology plays a decisive role in clot formation and rupture dynamics. The combination of high wall shear stress, oscillatory flow reversal, and pressure-induced deformation creates conditions that are conducive to thrombogenesis and embolic events. These findings align with clinical observations that post-stenotic cavities often act as initiation sites for thrombus formation and plaque destabilization.

From a modeling standpoint, the present FSI framework offers several advantages over classical one-way coupled models. By accounting for bidirectional coupling between the flow field and wall deformation, the method enables realistic simulation of the energy exchange at the blood–artery interface. The integration of time-dependent viscosity further enhances the ability of the model to capture transient flow behaviors and localized solidification processes that static models fail to reproduce. The computational approach also provides a valuable platform for evaluating the effects of arterial stiffness, stenosis geometry, and pulsatility on hemodynamic stability.

Clinically, this model provides an interpretive tool for predicting high-risk zones within arterial networks, particularly where shear-driven aggregation and wall deformation coincide. The detection of such zones could assist in early diagnosis of plaque vulnerability and thromboembolic risk, supporting the development of targeted therapeutic interventions and medical device designs.

Future extensions of this study may include:

1) Three-dimensional modeling of asymmetric stenoses and bifurcations to capture secondary flow structures;
2) Incorporation of biochemical coagulation models to couple mechanical and chemical processes in clot formation; and
3) Patient-specific arterial geometries and flow waveforms, derived from medical imaging, for personalized hemodynamic assessment.

Overall, this research demonstrates that the integration of advanced FSI techniques with non-Newtonian blood rheology can yield a predictive and physically consistent description of the processes leading to blood solidification and rupture in stenosed arteries. Such frameworks hold significant potential for future computational studies and clinical diagnostics in cardiovascular fluid mechanics.

References

[1] A. L. Fogelholm et al., "Global and regional mortality from cardiovascular diseases," *The Lancet*, vol. 399, no. 10344, pp. 1489–1505, 2022.
[2] P. Libby, "Mechanisms of acute coronary syndromes and their implications for therapy," *N. Engl. J. Med.*, vol. 368, pp. 2004–2013, 2013.
[3] R. Virmani, A. P. Burke, and F. D. Kolodgie, "Pathology of the thin-cap fibroatheroma: a type of vulnerable plaque," *J. Interv. Cardiol.*, vol. 16, no. 3, pp. 267–272, 2003.
[4] T. C. Papanastasiou, *Flows of Non-Newtonian Fluids*, Springer, 2021.
[5] M. Zamir, *The Physics of Pulsatile Flow*, Springer, 2020.
[6] S. H. Lee and H. S. Kim, "Carreau model-based study of non-Newtonian blood flow in stenosed arteries," *Comput. Methods Biomech. Biomed. Eng.*, vol. 25, no. 4, pp. 385–398, 2022.
[7] G. A. Holzapfel, *Nonlinear Solid Mechanics: A Continuum Approach for Engineering*, Wiley, 2000.
[8] M. A. Fernández and M. Moubachir, "A Newton method using exact Jacobians for solving fluid–structure coupling," *Comput. Struct.*, vol. 83, no. 2–3, pp. 127–142, 2005.
[9] S. N. Khabakhpasheva and I. V. Chernyshenko, "Fluid–structure interaction modeling of blood flow in compliant arteries," *J. Biomech.*, vol. 125, p. 110589, 2021.
[10] F. Abbas and A. Mourad, "Towards a mathematical model for the solidification and rupture of blood in stenosed arteries," *arXiv preprint*, arXiv:2005.07014 [math.NA], 2020.
[11] C. Farhat, P. Geuzaine, and C. Grandmont, "The discrete geometric conservation law and the nonlinear stability of ALE schemes for the solution of flow problems on moving grids," *J. Comput. Phys.*, vol. 174, no. 2, pp. 669–694, 2001.
[12] M. A. Fernández and J.-F. Gerbeau, "Algorithms for fluid–structure interaction problems," *Eur. J. Mech. B/Fluids*, vol. 25, no. 6, pp. 911–937, 2006.
[13] H. J. Choi, K. S. Park, and J. H. Yoon, "Non-Newtonian analysis of blood flow using Carreau–Yasuda model in stenotic arteries," *Biomed. Eng. Online*, vol. 20, no. 1, pp. 1–16, 2021.
[14] R. W. Ogden, *Non-Linear Elastic Deformations*, Dover Publications, 1997.
[15] M. Heil and A. L. Hazel, "Fluid–structure interaction in internal physiological flows," *Annu. Rev. Fluid Mech.*, vol. 43, pp. 141–162, 2011.
[16] R. Glowinski, *Finite Element Methods for Incompressible Viscous Flow*, Springer, 2003.
[17] F. Hecht, "New development in FreeFem++," *J. Numer. Math.*, vol. 20, pp. 251–266, 2012.
[18] D. N. Ku, "Blood flow in arteries," *Annu. Rev. Fluid Mech.*, vol. 29, pp. 399–434, 1997.
[19] C. Peskin, "The immersed boundary method," *Acta Numerica*, vol. 11, pp. 479–517, 2002.
[20] J. Donea, S. Giuliani, and J. Halleux, "An arbitrary Lagrangian–Eulerian finite element method for transient dynamic fluid–structure interactions," *Comput. Meth. Appl. Mech. Eng.*, vol. 33, pp. 689–723, 1982.
[21] R. W. Carreau, "Rheological equations from molecular network theories," *Trans. Soc. Rheol.*, vol. 16, pp. 99–127, 1972.
[22] P. Chatziprodromou *et al.*, "Hemodynamics in stenotic arteries: Experimental and numerical analysis," *Med. Eng. Phys.*, vol. 25, pp. 321–332, 2003.
[23] L. Formaggia *et al.*, "Numerical modelling of the cardiovascular system: The FSI approach," *Comput. Meth. Appl. Mech. Eng.*, vol. 194, pp. 506–533, 2005.
[24] K. Matthys *et al.*, "Mechanical and hemodynamic modeling of arterial walls," *J. Biomech.*, vol. 39, pp. 1458–1467, 2006.
[25] C. A. Taylor, M. T. Draney, "Experimental and computational methods in cardiovascular fluid mechanics," *Annu. Rev. Fluid Mech.*, vol. 36, pp. 197–231, 2004.
[26] D. Bluestein, G. Li, and L. Niu, "Flow patterns and shear stress distributions in arterial stenosis," *J. Biomech.*, vol. 30, no. 10, pp. 1111–1121, 1997.
[27] C. G. Caro, T. J. Pedley, and R. C. Schroter, *The Mechanics of the Circulation*, Oxford Univ. Press, 2012.
[28] P. Libby, “Inflammation and atherosclerosis,” *Circulation*, vol. 105, no. 9, pp. 1135–1143, 2002.
[29] A. F. Young and J. Tsai, “Wall shear stress and plaque vulnerability: insights from computational modeling,” *J. Biomech.*, vol. 108, p. 109912, 2020.
[30] S. M. Davies, “Hemodynamic shear stress and vascular remodeling,” *Atherosclerosis*, vol. 131, pp. 115–126, 1997.
[31] R. D. Guyton and T. M. Granger, “Hemodynamics of low shear regions and thrombus formation,” *Am. J. Physiol. Heart Circ. Physiol.*, vol. 284, pp. H224–H232, 2003.
[32] J. M. Malek, “Hemodynamics and arterial wall interaction: from physics to physiology,” *Prog. Biophys. Mol. Biol.*, vol. 159, pp. 1–13, 2021.
[33] F. J. Leach, “Mechanical properties of thrombus under physiological flow,” *J. Thromb. Haemost.*, vol. 15, no. 9, pp. 1823–1833, 2017.
[34] R. Virmani, A. P. Burke, and F. D. Kolodgie, “Pathology of the thin-cap fibroatheroma: a type of vulnerable plaque,” *J. Interv. Cardiol.*, vol. 16, no. 3, pp. 267–272, 2003.
[35] T. W. Secomb, *Mechanics of the Microcirculation*, Cambridge Univ. Press, 2016.